Journal of Materials Chemistry A

PAPER

View Article Online
View Journal | View Issue

Cite this: *J. Mater. Chem. A*, 2018, **6**, 5143

From a Au-rich core/PtNi-rich shell to a Ni-rich core/PtAu-rich shell: an effective thermochemical pathway to nanoengineering catalysts for fuel cells†

Aolin Lu,[ab] Zhi-Peng Wu,[b] Binghui Chen,[a] Dong-Liang Peng,[a] Shan Yan,[b] Shiyao Shan,[b] Zakiya Skeete,[b] Fangfang Chang,[b] Yuanzhi Chen,[a] Hongfei Zheng,[a] Deqian Zeng,[a] Lefu Yang,[a] Anju Sharma,[b] Jin Luo,[b] Lichang Wang,[c] Valeri Petkov[d] and Chuan-Jian Zhong*[b]

A major challenge in the design of nanocatalysts containing noble metals is the ability to engineer their relative surface composition and structure so that their catalytic activity and stability can be enhanced with minimum use of the noble metals. We demonstrate here this ability by an effective thermochemical pathway enabling us to control the structural evolution of fuel cell nanocatalysts from an Au-rich core/PtNi-rich shell to a Ni-rich core/PtAu-rich shell. The synthesis starts from the introduction of a third low-cost transition metal (nickel) into AuPt nanoparticles through a facile one-pot synthesis followed by thermochemical and electrochemical treatments. By exploiting the surface free energy differences among Au, Pt and Ni, the as-synthesized Au-rich core/PtNi-rich shell structure is transformed into a Ni-rich core/PtAu-rich shell structure, producing a significant multifunctional synergy in comparison with bimetallic PtAu nanoparticles. The surface enrichment of PtAu with slightly segregated Au, along with shrinking of Pt–Pt distances, is shown to enhance the dehydrogenation of methanol and effectively remove the surface carbonaceous species. The surface Au atoms facilitate maneuvering of the electrons in the oxidation reactions, whereas the positively charged PtAu rich surface resulted from electrochemical treatment enhances the oxidation activity. The mass activity of the nanocatalysts is shown to maximize as a function of Ni doping. The result is further supported by computational analysis of the adsorption energy of methanol on the nanoclusters, revealing that the increased catalytic activity correlates well with the decreased adsorption energy. These findings demonstrate an unprecedented ability to invert the core–shell structure of the as-synthesized nanocatalysts for electrocatalytic enhancement, which has significant implications for the design of noble metal containing nanocatalysts for fuel cells.

Received 2nd January 2018
Accepted 8th February 2018

DOI: 10.1039/c8ta00025e

rsc.li/materials-a

1. Introduction

Two of the major problems in the development of direct methanol oxidation fuel cells (DMFCs) include poor activity of the anode catalysts and "methanol crossover" to the cathode electrode,[1,2] which lead to a loss of about one-third of the available energy at the cathode and another one-third at the anode. For the anode reaction of DMFCs, Pt is one of the most active catalysts, but has a propensity to be poisoned by CO-like intermediate species.[3–5] To address this problem, the design of bimetallic AuPt nanostructures has been a focal point of increasing research interest,[6–8] which takes advantage of Au nanoparticles showing unprecedented catalytic activities for CO and methanol oxidation.[9–15] Moreover, alloying Pt with a second transition metal provides synergistic activities for the suppression of adsorbed poisonous species and the change of electronic band structure.[16–19] For the methanol oxidation reaction (MOR), Pt serves as the main site for dehydrogenation of methanol whereas Au provides surface-oxygenated species to favor their removal.[20–22] Au also functions as an electronic sink in promoting the oxidation reaction by draining negative charges.[23] Indeed, PtAu exhibits bifunctional synergy for the

[a]Department of Chemical and Biochemical Engineering, College of Chemistry and Chemical Engineering, Department of Materials Science and Engineering, College of Materials, Xiamen University, Xiamen 361005, China

[b]Department of Chemistry, State University of New York at Binghamton, Binghamton, NY 13902, USA. E-mail: cjzhong@binghamton.edu

[c]Department of Chemistry and Biochemistry, Southern Illinois University, Carbondale, Illinois 62901, USA

[d]Department of Physics, Central Michigan University, Mt Pleasant, Michigan 48859, USA

† Electronic supplementary information (ESI) available: Additional TEM images, size distribution analysis; EDS data; UV-vis spectra; TGA data; XRD data; CV data; plots in terms of size, ECA, MA, SA, and J_f/J_b; and comparison with literature data. See DOI: 10.1039/c8ta00025e

electrocatalytic MOR in alkaline electrolytes[24] and the oxygen reduction reaction in acidic electrolytes.[25,26] However, PtAu shows much lower activities for the MOR in acidic electrolytes[22,24] due to the suppression of surface-oxygenated species. The d band center of Pt has been considered to be shifted upward as a result of tensile strain by the expansion of the Pt lattice in the PtAu alloy (Au atoms are larger than Pt atoms), which however strengthens the adsorption of surface carbonaceous species.[16]

One of the major challenges in the design of nanocatalysts containing noble metals is the ability to engineer their relative surface composition and structure so that their catalytic activity and stability is enhanced with minimum use of the noble metals. Here we demonstrate an effective thermochemical pathway enabling the structural evolution of nanocatalysts from the as-synthesized Au-rich core/PtNi-rich shell to a Ni-rich core/PtAu-rich shell nanostructure. The concept of the introduction of a third transition base metal into the PtAu alloy stems from the consideration of lattice shrinking, d-band center lowering, and carbonaceous species adsorption weakening for Pt upon alloying with many transition base metals.[16] Moreover, base transition metals exhibit an oxyphilic character which would impact the surface partial charge characteristics for maneuvering the surface-oxygenated species. It is thus hypothesized that the introduction of Ni into the AuPt alloy could produce synergistic properties in terms of the interatomic distances, the partial surface charges and the surface oxyphilicity. Although several studies showed enhanced activity of electrochemical oxidation and the oxygen reduction reaction for ternary nanoparticles, *i.e.*, AuPtM (M = Ni, Fe, Cu, Co),[27–33] there have been no studies addressing how the doping of a third metal in PtAu nanoparticles influences the electrocatalytic properties. Earlier examples showed that Au-decorated PtFe nanocatalysts were effective for the formic acid oxidation reaction,[28] supporting the feasibility of the hypothesis. Considering that the stability of base metal alloyed catalysts could suffer from base metal leaching in acidic solutions, there have also been studies showing that rational selection of base metals could lower the d-band center, as shown by DFT calculations.[34,35] Indeed, enhanced activity and stability for the oxygen reduction reaction have been shown in recent studies of Au@PtNi and Ni@Au@PtNi prepared by two-step routes.[29,30,36] Also, significant suppression of the carbonaceous poisoning for the electrocatalytic MOR is reported by depositing Au on PtNi nanoparticles.[37] However, how the nanostructure is controlled in terms of different metal composition, phase structure, surface structure and surface-oxygenated species for enhancing the catalytic activities remains unknown. In the one-pot synthesis route, the reduction of the Au precursor could proceed to PtNi (Scheme S1†), favoring an Au@PtNi core–shell structure.[29,30,36] This is undesired if the catalytic synergy of noble metal Au is needed in the catalytic reaction. Based on the calculated surface energy differences, Au (0.0554 eV $Å^{-2}$) < fcc Pt (0.1035 eV $Å^{-2}$) < fcc Ni (0.1272 eV $Å^{-2}$), (the (111) plane of the fcc structure),[38] we hypothesize that under controlled thermochemical conditions for an Au-rich core/PtNi-rich shell structure, Au could diffuse from the core to the shell and Ni from the shell to the core, leading to the formation of a Ni-rich core/PtAu-rich shell structure (Scheme 1). We demonstrate for the first time in this work that the Au-rich core/PtNi-rich shell structure formed upon introduction of Ni into AuPt in a controllable ratio can be reconstructed to form a Ni-rich core/PtAu-rich shell structure with an enhanced catalytic synergy.

2. Experimental section

2.1. Chemicals

Platinum(II) acetylacetonate ($Pt(acac)_2$, 97%), nickel(II) acetylacetonate ($Ni(acac)_2$, anhydrous, >95%) and gold chloride hydrate ($HAuCl_4$) were purchased from Alfa Aesar. 1,2 hexadecanediol (CH_3–$(CH_2)_{13}$–CH(–OH)–CH_2–OH, 90%), octadecene ($CH_3(CH_2)_{15}CH{=}CH_2$, 99%), oleylamine ($CH_3(CH_2)_7CH{=}CH(CH_2)_8NH_2$, 70%), oleic acid ($CH_3(CH_2)_7CH{=}CH(CH_2)_7$-COOH, 99%) and Nafion solution (5 wt%) were purchased from Aldrich. Carbon black (Vulcan XC-72) was obtained from Cabot. The Pt/C catalyst (Pt loading 20%) was obtained from E-tek (BASF). Water was purified with a Millipore Milli-Q water system. Other solvents such as ethanol, hexane and perchloric acid were purchased from Fisher Scientific. All chemicals were used as received.

2.2. Catalyst preparation

Typically, the synthesis of PtAuNi nanoparticles involved mixing three metal precursors, 0.3 mmol $Pt(acac)_2$, 0.4 mmol $Ni(acac)_2$ and 0.14 mmol $HAuCl_4$, with 20 mL octadecene solvent. 1,2-Hexadecanediol was added as a reducing agent and oleic acid and oleylamine as capping agents. The temperature was increased rapidly (16 °C min^{-1}) to 230 °C with reflux for 1 h and then cooled to room temperature. The NPs were precipitated out by adding ethanol. The PtAuNi NPs were then dispersed in hexane solvent for further use. $Pt_{56}Au_{44}$ nanoparticles were synthesized with the same route using 0.3 mmol $Pt(acac)_2$ and 0.2 mmol $HAuCl_4$. $Pt_{38}Au_{62}$ nanoparticles were synthesized using 0.2 mmol $Pt(acac)_2$ and 0.3 mmol $HAuCl_4$.

The PtAuNi nanoparticles were supported on carbon black and subjected to the subsequent thermochemical treatment. The preparation of carbon-supported nanoparticles followed our earlier protocols[39] with slight modifications. The thermochemical treatment involved three different conditions, (1) 260 °C in 20 vol% O_2 for 30 min; (2) 177 °C in 20 vol% O_2 for 12 hours; and (3) 400 °C in 15 vol% H_2 for 60 min, to remove the capping agent and anneal the particles.[27,40]

Transmission electron microscopy (TEM) measurements were carried out on a JEOL JEM 2010F with an acceleration voltage of 200 kV and a routine point-to-point resolution of 0.194 nm. High resolution TEM (HR-TEM) was performed on a TECNAI F-30 transmission electron microscope equipped with a scanning TEM (STEM) unit and a high-angle annular dark-field (HAADF) detector operated at 300 kV, which had a highest line resolution of 0.100 nm. For TEM measurements, the samples were diluted in hexane solution and were drop cast onto a carbon-coated copper grid followed by solvent evaporation in air.

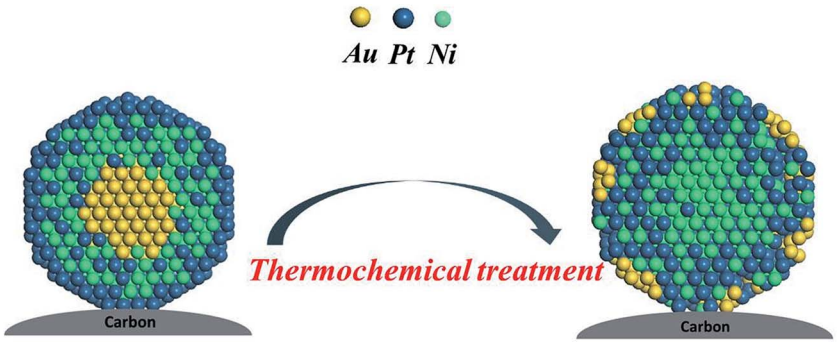

Scheme 1 Reconstruction from the Au-rich core/PtNi-rich shell structure to the Ni-rich core/PtAu-rich shell structure under controlled thermochemical conditions.

Ultraviolet-visible spectra were acquired with an HP 8453 spectrophotometer. The spectra were collected in the range of 300–1000 nm.

Inductively Coupled Plasma-Optical Emission Spectroscopy (ICP-OES) was performed on a PerkinElmer 2000 DV ICP-OES instrument utilizing a Meinhard nebulizer coupled to a cyclonic spray chamber to increase the analytic sensitivity with the following parameters: 18.0 L of Ar min^{-1}; auxiliary 0.3 L of Ar min^{-1}; nebulizer 0.73 L of Ar min^{-1}; power 1500 W; peristaltic pump rate 1.40 mL min^{-1}. Laboratory check standards were analyzed for every 6 or 12 samples and the instrument was recalibrated if the check standards were not within ±5% of the initial concentration.

Thermogravimetric analysis (TGA) was performed on a Perkin-Elmer Pyris 1-TGA.

X-ray powder diffraction (XRD) was used to characterize the alloying structures. XRD data were collected from 30 to 90° for 2θ with a step size of 0.04° at room temperature on a Philips X'pert PW 3040 MPD diffractometer using Cu Kα line (λ = 1.5418 Å); the data were compared to the XRD database of the International Centre for Diffraction Data (ICDD) for phase identification.

X-ray photoelectron spectroscopy (XPS) was performed *ex situ* using a Physical Electronics Quantum 2000 scanning ESCA Microprobe. This instrument was equipped with a focused monochromatic Al Kα X-ray (1486.7 eV) source for excitation, a spherical section analyzer and a 16-element multichannel detection system. The X-ray beam was approximately 100 μm in diameter. It was rastered over a 1.4 mm by 0.2 mm rectangular spot on the sample. During rastering, the incident X-ray beam was normal to the sample while the X-ray detector was tilted at 45° away from the normal. The binding energy (BE) of the chemical species adsorbed at the NP surface was calibrated using the C 1s peak at 284.8 eV as an internal standard. The percentages of the individual elements detected were determined by analyzing the areas of the respective peaks.

2.3. Preparation of working electrodes

Glassy carbon (GC) disks (geometric area: 0.196 cm^2) were polished with 0.03 μm Al_2O_3 powders, followed by careful rinsing with deionized water. Briefly, the catalyst ink (1 mg mL^{-1}) was prepared by ultrasonicating a solution of 5 mg catalysts, 4.5 mL distilled water, 0.25 mL isopropanol and 0.25 mL 5 wt% Nafion for 20 min. The as-prepared ink was aged in a dark environment for 3 weeks and then ultrasonicated for 20 min. Then, 10 μL of the ink was deposited onto the polished glassy carbon disk of 5 mm diameter, followed by drying under ambient conditions.

2.4. Electrochemical measurements

Cyclic voltammetry (CV) measurements were performed using a computer-controlled electrochemical analyzer (CHI 600A). The experiments were conducted in three-electrode electrochemical cells at room temperature in 0.1 M $HClO_4$. The reference electrode was a silver–silver chloride electrode in saturated KCl (Ag/AgCl (Sat'd KCl)). The potential can be calibrated to the reversible hydrogen electrode (RHE) using the following equation: (E(RHE) = E(Ag/AgCl) + 0.0591 pH + E^0(Ag/AgCl)). E^0(Ag/AgCl) is measured to be 0.192 V. Cyclic voltammetric sweeps were run at 50 mV s^{-1} (−0.20–1.25 V or −0.20–1.39 V). The MOR was performed in 0.1 M $HClO_4$ containing 0.5 M CH_3OH between −0.20 V and 0.96 V.

2.5. Computational modeling

Ab initio calculations were carried out using DFT as implemented in the Dmol3 program coming as a part of Materials Studio software (Accelrys Inc.).[41] Full geometry optimizations were performed for all model atomic configurations tested in this work, in which all atoms were fully relaxed. The configurations included small PtAuNi clusters. The interactions between the model atomic configurations of the clusters and the CH_3OH molecule were explored. The energy of adsorption of CH_3OH on the PtAuNi cluster was used as a measure of the strength of CH_3OH adsorption. It was calculated as follows:

$$E_{ads} = -(E_{CH_3OH\text{–}metal} - E_{metal} - E_{CH_3OH}),$$

where, $E_{CH_3OH\text{–}metal}$, E_{metal} and E_{CH_3OH} are the total energy for the CH_3OH–metal complex, the isolated atomic configuration of the cluster, and the isolated CH_3OH molecule, respectively.

3. Results and discussion

3.1. Compositions and morphologies

On the basis of our previous work on the MOR activity of Pt_n-Au_{100-n} in alkaline electrolyte which showed a gradual increase in activity with decreasing n, reaching a maximum at $n \sim 20$,[20] here we focused on Pt_nAu_{100-n} NPs with an intermediate Pt percentage ($n \sim 40$) to assess the influence on the activity by replacing a fraction of Au with Ni. A typical example of such a composition was $Pt_{40}Au_xNi_{60-x}$. The actual trimetallic/bimetallic composition of the NPs was determined by the ICP-OES technique, which gave $Pt_{34}Au_2Ni_{64}$ (Sample a), $Pt_{38}Au_8Ni_{55}$ (Sample b), $Pt_{39}Au_{18}Ni_{43}$ (Sample c), $Pt_{40}Au_{30}Ni_{30}$ (Sample d), $Pt_{56}Au_{44}$ (Sample e), and $Pt_{38}Au_{62}$ (Sample f). The mass and atomic percentages of Pt for $Pt_{56}Au_{44}$ and $Pt_{38}Au_{62}$ are similar to those of the other four $Pt_{\sim 40}Au_xNi_{\sim 60-x}$ samples. Fig. 1 shows a plot of Pt, Au and Ni compositions in $Pt_{\sim 40}Au_xNi_{\sim 60-x}$ NPs as a function of nominal Au feeding in the synthesis. The atomic Au% in the NPs was very close to the Au% in the synthesis feeding. Au and Ni atomic percentages showed a linear relationship with the Au feeding percentage. The Ni% decreased and the Pt% in the NPs slightly increased with increasing Au feeding percentage.

The TEM images of the as-synthesized NPs show a spherical morphology with a size distribution of 8.7 ± 2.5 nm for Sample e (Fig. 2A), 7.0 ± 1.2 nm for Sample d (Fig. 2B), and 8.7 ± 2.0 nm for Sample c (Fig. 2C, Fig. S1†). The HR-TEM image (Fig. 2C inset) reveals a distinctive core–shell structure. As shown in Fig. 2D and E for the NPs synthesized by decreasing the Au : Ni ratio, there is a propensity of forming branching structures. In the absence of the Au precursor, $Pt_{32}Ni_{68}$ nanoflowers were obtained with a small size (Fig. S3†).

While the lattice fringes from the central part of the particles are complicated by the surface layers of the core, the lattice fringes in the edge of the nanoparticles are not, and thus the difference in lattice fringes measured between the center and the edge should reflect the difference of the core and shell. The HR-TEM image (Fig. 2F) of the as-prepared $Pt_{39}Au_{18}Ni_{43}$ NPs reveals a dark core with lattice fringes of 0.23 nm corresponding to the Au (111) plane, and a light shell with lattice fringes of 0.22 nm corresponding to the (111) plane of the PtNi-abundant phase. The PtAuNi core–shell structure formation was supported by UV-vis data (see Fig. S2†) which showed no surface plasmonic band corresponding to Au NPs. This is similar to that observed for AuPt core–shell nanoparticles,[24] reflecting the depression of the Au SP band by Pt–Ni shells. The standard (111) lattice spacing is 0.235, 0.226 and 0.204 nm for fcc Au, Pt and Ni phases. The interplanar distances near the shell are close to the lattice constant of Pt, suggestive of Pt surface enrichment. The nanospheres display (111)-dominant facets (interplanar distance: 0.21–0.23 nm) and branches with (200) dominant facets (interplanar distance: ~0.19 nm) (see Fig. S4†). A crystalline Au core (interplanar distance: 0.23 nm) and a PtNi-abundant shell (interplanar distance: 0.22 nm and 0.21 nm) are revealed in the initial HR-TEM of a spherical PtAuNi core–shell NP (Fig. 2G). The Au core exhibits an increased crystallinity after exposure to a high-energy electron beam for 15 min (Fig. 2H), at which the difference of interatomic distances between the core and the shell became smaller. The electron beam induced heating in a vacuum, similar to thermal treatment, and led to Au surface enrichment.

For $Pt_{39}Au_{18}Ni_{43}$/C after thermochemical treatment at 400 °C under H_2 (400 °C/H_2), the particles are well dispersed on the carbon (Fig. 3A). The corresponding selected area electron diffraction (SAED) pattern (Fig. 3A inset) taken from a randomly distributed region reveals (111), (200) and (220) diffraction rings of the fcc structure. The HR-TEM image (Fig. 3B) of a single particle shows the surface Au-rich domains with an interatomic distance of 0.23 nm, different from the interplanar distance of 0.21 nm in the core regions. Some of the branched NPs were shown to evolve into spherical NPs upon 400 °C/H_2 treatment (Fig. S5†). Both the (200) lattice fringe with an interplanar distance of 0.19 nm and the (111) lattice fringe with an interatomic distance of 0.22 nm remain unchanged after 400 °C/H_2 treatment (Fig. 3C).

The Au-rich core/PtNi-rich shell structure of the as-prepared $Pt_{39}Au_{18}Ni_{43}$/C was also supported by EDS point data which revealed that the core has a composition of $Pt_{46}Au_{39}Ni_{15}$ and the shell has a composition of $Pt_{64}Au_{10}Ni_{25}$ (Fig. S6†). Fig. 4 shows a representative set of HAADF-STEM images and the elemental mapping of 400 °C/H_2 treated $Pt_{39}Au_{18}Ni_{43}$/C. The three elements, Pt, Au and Ni, were all detectable for all individual nanoparticles. Due to the lack of enough resolution of the EDS mapping, the data do not effectively detect the enrichment of a specific element in the NP. However, as shown in Fig. 4F, the analysis of the line profile of the 20 nm sized dimeric particles supported the Ni-rich cores. For the smaller ~10 nm particle in the red rectangular region (Fig. 4A), EDS data taken from the core site gave a composition of "$Pt_{10}Au_5Ni_{85}$", which is different from the bulk composition of $Pt_{36}Au_{18}Ni_{46}$ (see Fig. S8†). This result is consistent with the finding of HR-TEM analysis showing that the 400 °C/H_2 treated $Pt_{39}Au_{18}Ni_{43}$/C catalyst features a Ni-rich core/PtAu-rich shell structure. EDS data of the

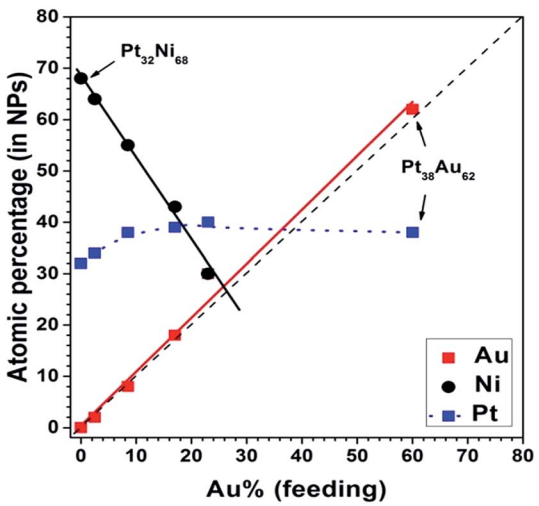

Fig. 1 Plots of Au and Ni atomic percentages of $Pt_{\sim 40}Au_xNi_{\sim 60-x}$/C as a function of nominal Au feeding in terms of the atomic percentage.

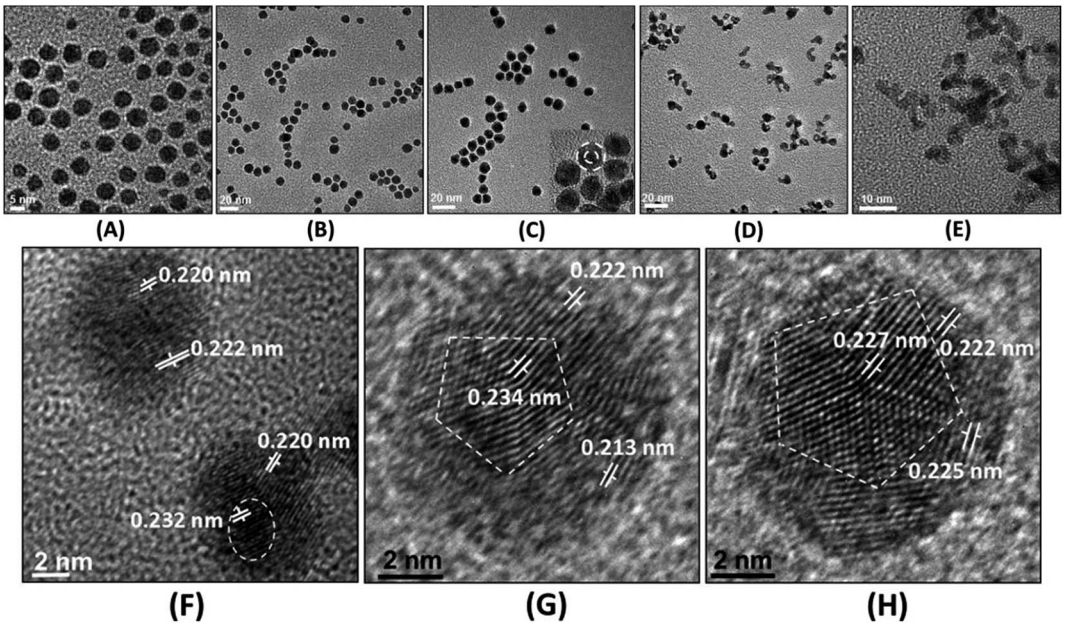

Fig. 2 TEM images of the as-prepared: (A) $Pt_{56}Au_{44}$, (B) $Pt_{40}Au_{30}Ni_{30}$, (C) $Pt_{39}Au_{18}Ni_{43}$, (inset: the high-magnification TEM image showing the contrast of the Au core and PtNi shell), (D) $Pt_{37}Au_8Ni_{55}$, (E) $Pt_{34}Au_2Ni_{64}$ (F) high-resolution TEM image showing the lattice fringes of the Au-rich core ((111) lattice space: 0.232 nm) and PtNi-rich shell ((111) lattice space: 0.220 nm and 0.222 nm). HR-TEM image of the PtAuNi core–shell structure before (G) and after (H) exposure to TEM electron beams for 15 min.

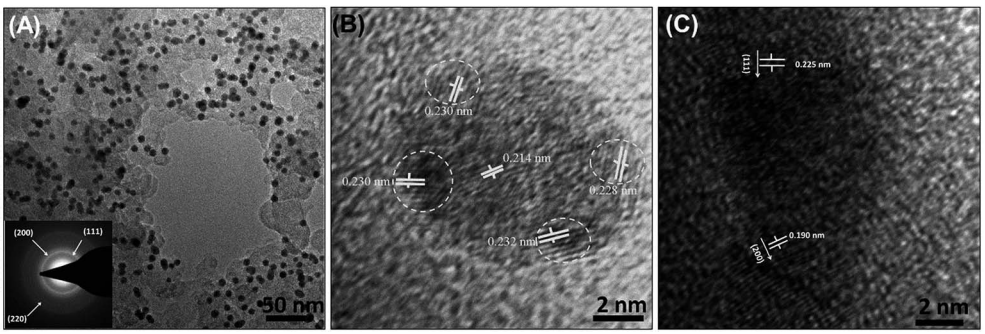

Fig. 3 (A) TEM image of 400 °C/H_2 treated $Pt_{39}Au_{18}Ni_{43}$/C (inset: the corresponding SAED patterns), (B) HR-TEM image of a single particle with an Au-rich surface domain ((111) lattice space: 0.230 nm and 0.232 nm) and PtNi-rich domain (lattice space: 0.214 nm), and (C) HR-TEM image of 400 °C/H_2 treated $Pt_{37}Au_8Ni_{55}$/C.

260 °C/O_2 treated $Pt_{39}Au_{18}Ni_{43}$/C catalyst showed a composition of "$Pt_{43}Au_{18}Ni_{28}$" in the core and "$Pt_{37}Au_{14}Ni_{47}$" in the shell (Fig. S7†), indicative of an enrichment of Ni in the shell. Considering that electron energy loss spectroscopy (EELS) has the ability to detect the composition at 0.5–2 nm of the surface, we plan to use the EELS technique to examine the samples in the near future to provide an additional piece of information to further support the core–shell nanostructure.

3.2. Phase properties

The XRD pattern of 400 °C/H_2 treated $Pt_{\sim 40}Au_xNi_{\sim 60-x}$ showed an fcc-type structure (Fig. S9A†). The structure is influenced by thermochemical treatment (Fig. S9B†). As shown in Fig. 5A, the (111) peak shifts positively with the increase of Ni composition. In comparison with those reported for the as-synthesized PtAuFe[42] and PtAu,[6] the characteristics of the Au core in our as-synthesized $Pt_{39}Au_{18}Ni_{43}$ NPs were detectable. Catalysts derived from $Pt_{39}Au_{18}Ni_{43}$/C (denoted as Sample c) treated at three different temperatures, 260 °C/O_2 (denoted as Sample c-1), 177 °C/O_2 (denoted as Sample c-2), and 400 °C/H_2 (denoted as Sample c-3) were examined (Fig. 5B). By deconvoluting the XRD peaks for the untreated $Pt_{39}Au_{18}Ni_{43}$ NPs (Sample c), the left shoulder of the main Pt (111) peak can be ascribed to the (111) peak of the Au core. In terms of Au segregation and the Pt-based alloy phase during thermochemical treatment, the XRD spectra between 34° and 50° were deconvoluted into three peaks: an Au (111) peak at 38.19° (red curve), a Pt alloy (111) peak with a shift (blue curve), and a peak representing the overlap of Au (200) and the Pt alloy (200) (green curve). The deconvolution reveals an interesting trend: after O_2 treatment at 177 °C, the Au (111) peak was suppressed and the Pt alloy (111) peak shifted negatively

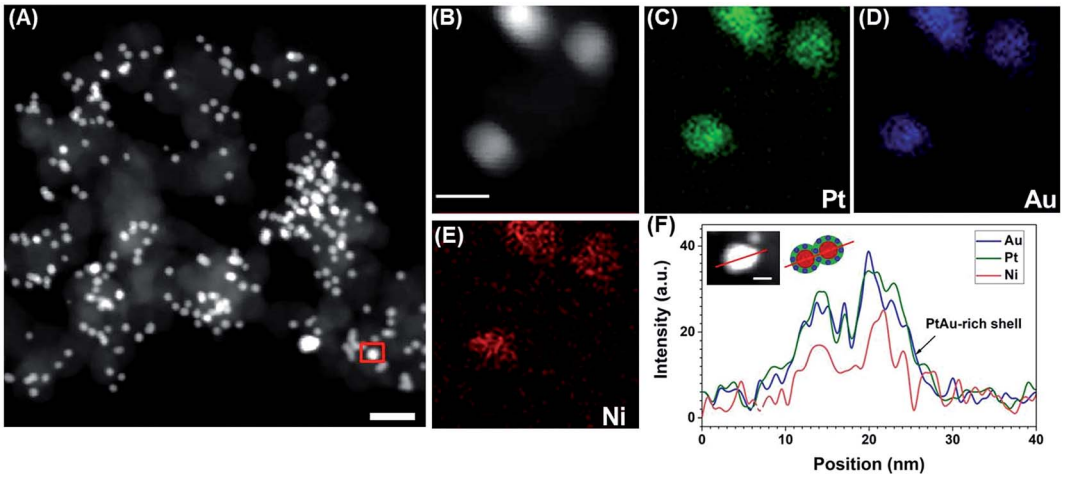

Fig. 4 (A) HAADF-STEM image of 400 °C/H_2 treated $Pt_{39}Au_{18}Ni_{43}$/C. (Scale bar: 50 nm): composition analysis: core composition in the red rectangular region: $Pt_{10}Au_5Ni_{85}$ and bulk composition: $Pt_{36}Au_{18}Ni_{46}$ (see Fig. S8† in detail); (B–F) elemental mapping showing (C) Pt, (D) Au, and (E) Ni. (Scale bar: 10 nm). (F) Line profile of a larger-sized dimeric particle (inset: HAADF-STEM image and the dimeric model of the particles).

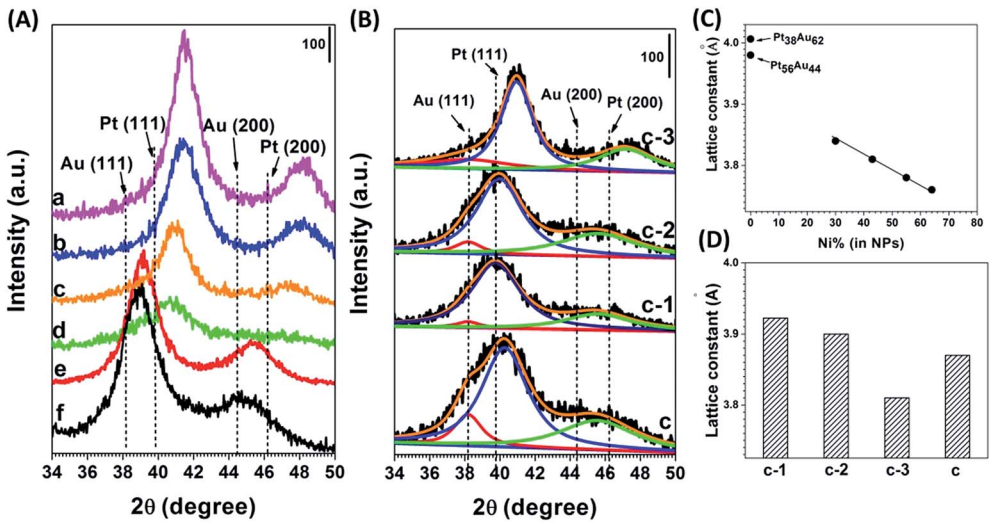

Fig. 5 (A) XRD patterns of 400 °C/H_2 treated (a) $Pt_{34}Au_2Ni_{64}$/C, (b) $Pt_{37}Au_8Ni_{55}$/C, (c) $Pt_{39}Au_{18}Ni_{43}$/C, (d) $Pt_{40}Au_{30}Ni_{30}$/C, (e) $Pt_{56}Au_{44}$/C, and (f) $Pt_{38}Au_{62}$/C. (B) Deconvoluted XRD patterns of $Pt_{39}Au_{18}Ni_{43}$/C: (c) as-prepared, and treated: (c-1) 260 °C/O_2, (c-2) 177 °C/O_2, and (c-3) 400 °C/H_2. (C) Plot of the lattice constant as a function of Ni% for 400 °C/H_2 treated $Pt_{\sim 40}Au_xNi_{\sim 60-x}$/C. (D) Comparison of lattice constants for c, c-1, c-2, and c-3.

from 40.27° to 39.96°. For Sample c-1, the Au (111) peak was weaker while the Pt alloy (111) peak shifted more negatively to 39.75°. The result indicates that PtAu alloying is favored by O_2 treatment, with an expansion of the lattice space. For Sample c-3, the Pt alloy (111) peak shifted positively to 40.91°, promoting the PtNi alloy with a lattice shrinking. Our previous study showed a relative difference ($\Delta a/a$) in the lattice parameter of about 1.0, 1.4 and 3.0% for Pt, $Pt_{45}Co_{55}$, and $Pt_{50}Co_{25}Ni_{25}$ NPs after O_2 and H_2 treatments.[43] Here, $Pt_{39}Au_{18}Ni_{43}$/C exhibits a significant difference in the lattice parameter of about 2.9% between the H_2 and O_2 treated samples.

The ratio of Au and Pt alloy (111) peaks represents the ratio of segregated Au *vs.* the Pt alloy phase. For the untreated $Pt_{39}Au_{18}Ni_{43}$/C (denoted as Sample c), the ratio is 0.195. After 177 °C/O_2 treatment (denoted as Sample c-2), it decreased to 0.096 when the Au atoms in the core merged into the Pt alloy phase. For the 260 °C/O_2 treatment, the Au (111) peak is undetectable. The ratio for Sample c-3 is 0.274. Considering the broad Au (111) peak, Au segregation was promoted and converted to very small domains during H_2 treatment.

As demonstrated in Fig. 5C, the lattice constant for 400 °C/H_2 treated Samples a, b, c, d, e, and f as calculated using Bragg's law, was 0.376, 0.378, 0.381, 0.384, 0.398, and 0.401 nm, respectively. The fcc-type lattice constant for c-1, c-2, c-3, and c ($Pt_{39}Au_{18}Ni_{43}$/C) was 0.392, 0.390, 0.381, and 0.387 nm, respectively (Fig. 5D). The lattice constants of the four $Pt_{\sim 40}Au_xNi_{\sim 60-x}$/C samples show a linear relationship with Ni% except for $Pt_{38}Au_{62}$/C, demonstrating that Ni doping in PtAu

causes significant differences in the crystalline structure. PtNi alloys rather than PtAu alloys are more favored for PtAuNi NPs after 400 °C/H_2 treatment.

The average size of the segregated phase in the NPs can be estimated from the full width at half maximum of the Pt (111) peak using the Scherer equation:

$$L = \frac{k\lambda}{\beta \cos(\theta)}$$

As shown in Fig. S9C & D,† the size of the segregated Pt domains in 400 °C/H_2 treated $Pt_{40}Au_{30}Ni_{30}$/C is 2.2 nm, which is the smallest among the six compositions. For $Pt_{39}Au_{18}Ni_{43}$/C, the size of the segregated Pt domains is shown to decrease from 2.69 nm (as-synthesized) to 2.59 nm after 260 °C/O_2 treatment, but to increase to 3.95 nm in 400 °C/H_2 treatment.

To further substantiate the structural difference after thermochemical treatments in O_2 and H_2, the in-house XRD data collected with Ag K_α radiation (Fig. 6A) were transformed into PDF. As shown in Fig. 6B, the lattice constant of 400 °C/H_2 and 260 °C/O_2 treated $Pt_{40}Au_{20}Ni_{40}$/C is 3.853 and 3.954 Å with a difference of 2.6%. In comparison, the 400 °C/H_2 treated $Pt_{56}Au_{44}$/C exhibits a lattice constant of 3.944 Å. This result, in line with the previous findings, provides clear evidence for the lattice shrinking upon the introduction of Ni atoms into the PtAu NPs.

The loading of 400 °C/H_2 treated catalysts (Samples a, b, c, d, e, and f), as determined by TGA, was 23, 25, 23, 16, 27, and 20 wt%, respectively. The actual metal loadings of c-1 and c-2 were 18 and 17 wt%, respectively (Fig. S10†). Note that Sample c-3 with an Au-rich surface exhibited a higher degree of carbon burning than Samples c-1 and c-2, reflecting that Au is less active than Pt for the carbon burning reaction.

3.3. Electrocatalytic characteristics

CV for the 400 °C/H_2 treated $Pt_{\sim 40}Au_xNi_{\sim 60-x}$/C was performed in N_2 saturated 0.1 M $HClO_4$ (Fig. S11A†). A typical set of CV curves for the O_2 and H_2 treated $Pt_{39}Au_{18}Ni_{43}$/C is shown in Fig. 7A. The waves between −0.20 V and 0.15 V are characteristic of the hydrogen adsorption/desorption,[44] which are broader and weaker compared to those for Pt/C. The peaks observed at 0.25–0.65 V and 0.75–0.95 V correspond to the reduction of surface Pt and Au.[6,42] For the samples with a high Au content (*e.g.*, $Pt_{39}Au_{18}Ni_{43}$/C c-4, $Pt_{40}Au_{30}Ni_{30}$/C, $Pt_{56}Au_{44}$/C, and $Pt_{38}Au_{62}$/C), the current density showed an increase as the potential is increased above 0.85 V, corresponding to the oxidation of Au. For the spherical NPs (*e.g.*, $Pt_{39}Au_{18}Ni_{43}$/C, $Pt_{40}Au_{30}Ni_{30}$/C, and $Pt_{56}Au_{44}$/C), the reduction peak appears at 0.40 V, which showed a downshift to 0.35 V for $Pt_{38}Au_{62}$/C. For the branched NPs ($Pt_{34}Au_2Ni_{64}$/C and $Pt_{38}Au_8Ni_{55}$/C), it appears at about 0.47 V. The peak positions depend on the thermal treatment. For Samples c-1 and c-2, the reduction peak appeared at 0.43 and 0.45 V, respectively, which is higher than that of Sample c-3. The suppression of the Au reduction peak for O_2 treated $Pt_{39}Au_{18}Ni_{43}$/C was due to the absence of surface Au atoms. As a comparison, the 400 °C/H_2 and 260 °C/O_2 treated $Pt_{56}Au_{44}$/C catalysts were subjected to identical electrochemical measurements (Fig. S12A & B†).

The measurements of the MOR were carried out in N_2-saturated 0.1 M $HClO_4$ solution with 0.5 M MeOH (Fig. 7B, C, S11B & S13†). The well-defined peaks in the forward sweep correspond to the electrochemical oxidation of methanol with the formation of carbonaceous species adsorbed on the surface of the catalyst. The backward peaks reflect the oxidation of the carbonaceous species.[45] The MOR activity clearly depends on the composition and thermochemical and electrochemical treatments. The MOR properties of $Pt_{39}Au_{18}Ni_{43}$/C also vary significantly with treatment. Sample c-4 was 400 °C/H_2 treated $Pt_{39}Au_{18}Ni_{43}$/C subjected to potential cycling to a higher potential, and exhibited the strongest forward wave based on the Pt mass (Fig. 7B), whereas Sample c-3 showed the strongest MOR feature based on the surface active area (Fig. 7C). Both the O_2 and H_2 treated $Pt_{39}Au_{18}Ni_{43}$/C samples showed much higher activities than that of Pt/C.

The electrochemical active area (ECA) was measured by integration of the charges under the hydrogen adsorption waves between −0.20 V and 0.10 V. Fig. 8A shows ECA values of 400 °C/H_2 treated Sample a, b, c, d, e, f ($Pt_{\sim 40}Au_xNi_{\sim 60-x}$/C, $Pt_{56}Au_{44}$/C,

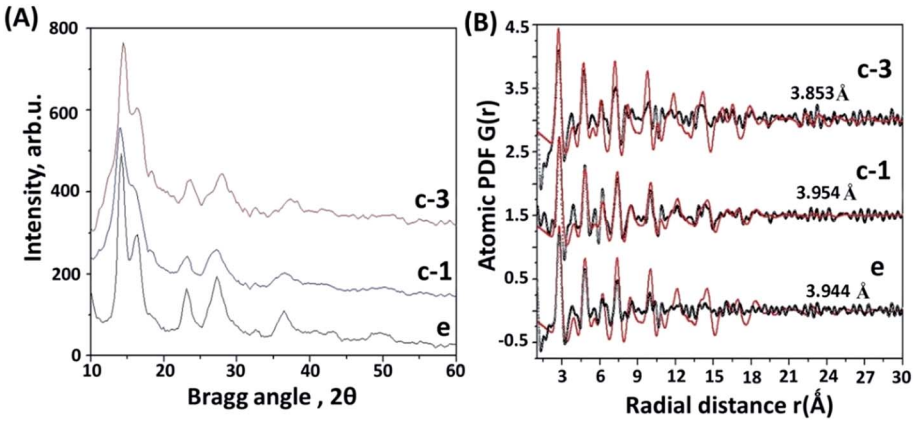

Fig. 6 (A) In-house data obtained with Ag K_α radiation and (B) the corresponding atomic PDFs for (e) 400 °C/H_2 treated $Pt_{56}Au_{44}$/C, (c-1) 260 °C/O_2, and (c-3) 400 °C/H_2 treated $Pt_{40}Au_{20}Ni_{40}$/C.

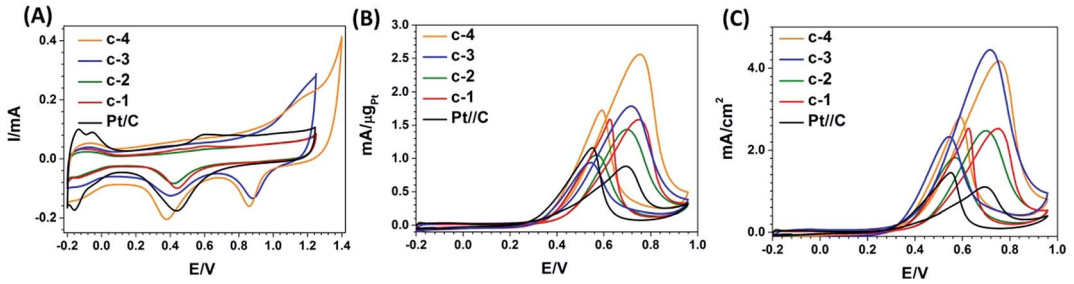

Fig. 7 CV curves for (c-1) 260 °C/O_2, (c-2) 177 °C/O_2, and (c-3) 400 °C/H_2 treated $Pt_{39}Au_{18}Ni_{43}$/C in comparison with Pt/C in (A) 0.1 M $HClO_4$ and (B and C) 0.1 M $HClO_4$ + 0.5 M MeOH in terms of mA μg^{-1} (Pt) and mA cm^{-2} (Pt). Sample c-4 (*i.e.*, 400 °C/H_2 treated $Pt_{39}Au_{18}Ni_{43}$/C) was subjected to potential cycling to a higher potential (1.39 V).

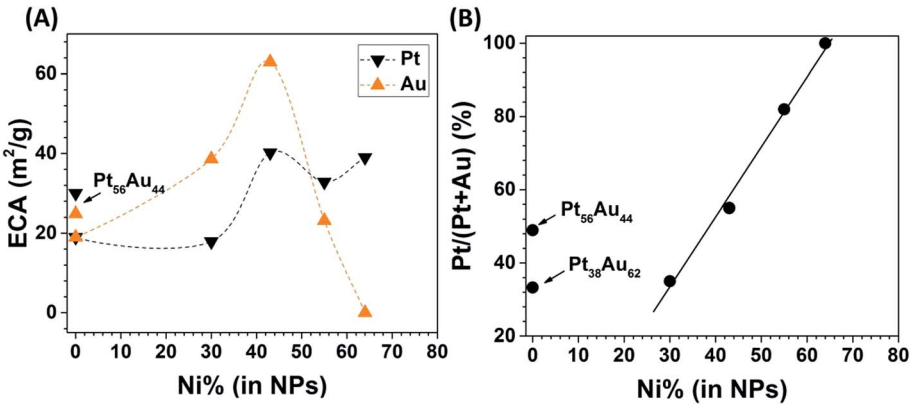

Fig. 8 Plots of ECA_{Pt} and ECA_{Au} values *vs.* Ni% for 400 °C/H_2 treated $Pt_{\sim 40}Au_xNi_{\sim 60-x}$/C and $Pt_{56}Au_{44}$/C per Pt or Au mass based on the hydrogen adsorption wave or Au reduction peak (A), and surface Pt/(Pt + Au) measured from the CV curve based on the Au reduction peak) *vs.* Ni% (B).

$Pt_{38}Au_{62}$/C), which are lower than that of Pt/C (80 m^2 g_{Pt}^{-1}). The ECA values for c-1, c-2 and c-3 ($Pt_{39}Au_{18}Ni_{43}$/C) are 63, 58 and 40 m^2 g_{Pt}^{-1}. Sample c-4 exhibits a higher ECA (65 m^2 g_{Pt}^{-1}) compared to Sample c-3 (Fig. S14†), reflecting an increased level of Ni leaching due to the potential cycling. The ECA values of 260 °C/O_2 and 400 °C/H_2 treated $Pt_{56}Au_{44}$/C are 47 and 30 m^2 g_{Pt}^{-1}, respectively, which increase to 48 and 60 m^2 g_{Pt}^{-1} after experiencing a higher potential of 1.39 V.

The ECA can also be evaluated based on surface Au, ECA_{Au}, using the following equation:

$$ECA_{Au} = \frac{Q}{340\ \mu C\ cm^{-2}\ m_{Au}}$$

where m_{Au} is the total mass of Au and Q is the total charge which can be evaluated using the area of the Au reduction peak. ECA_{Au} exhibits a maximum value of 65 m^2 g_{Au}^{-1} for 400 °C/H_2 treated $Pt_{39}Au_{18}Ni_{43}$/C (Fig. 8A). Due to the uniform distribution of Au atoms on the surface, $Pt_{39}Au_{18}Ni_{43}$/C showed the highest values of ECA_{Pt} and ECA_{Au}.

Considering the leaching of surface Ni in the process of potential cycling, the surface Pt : Au ratio is a critical parameter influencing the electrocatalytic properties. The surface Pt percentage of (Pt/(Pt + Au)) can be calculated using the area of hydrogen adsorption waves and the Au reduction peak[6] (Fig. S15†), which showed a linear relationship with atomic Ni% (Fig. 8B), except for $Pt_{56}Au_{44}$/C and $Pt_{38}Au_{62}$/C. In addition, as reflected by the values for the 400 °C/H_2 treated $Pt_{39}Au_{18}Ni_{43}$/C and $Pt_{56}Au_{44}$/C after potential cycling to 1.39 V (60% and 57%) being lower than that of 260 °C/O_2 treated $Pt_{56}Au_{44}$/C (81.25% and 82.9%) after potential cycling to 1.25 and 1.39 V, the O_2 treatment appeared to favor surface Pt enrichment than H_2 treatment.

As shown in Fig. 9A, the mass activities (MAs) at 0.6 V for the 400 °C/H_2 treated catalysts are compared with that of Pt/C, showing increases by a factor as high as 2.4 for Sample c-4. The specific activities (SA) at 0.6 V are also compared with that of Pt/C, showing increases by a factor as high as 4.0. For 400 °C/H_2 treated $Pt_{\sim 40}Au_xNi_{\sim 60-x}$/C, a higher Ni content tends to exhibit a higher activity. The 400 °C/H_2 treated catalysts with an intermediate atomic Ni% ($Pt_{39}Au_{18}Ni_{43}$) showed an enhanced activity, as evidenced by the maximum MA and SA at practically the same atomic Pt% in the NPs (Fig. 9B). Considering the activities of Au NPs[46] and AuPt[6,7] for the MOR, the high activity of the 400 °C/H_2 treated $Pt_{39}Au_{18}Ni_{43}$/C is believed to be linked to the high values of ECA_{Pt} and ECA_{Au}. The forward peak potential shows a similar trend in terms of MA and SA showing a maximum value at the intermediate Ni% (Fig. S16†).

The ratio of forward *vs.* backward maximum current (J_f/J_b) represents the tolerance of the catalyst to the carbonaceous species. As shown in Fig. 9C, the J_f/J_b values of 400 °C/H_2 treated catalysts, in comparison with that of Pt/C, are shown to decrease

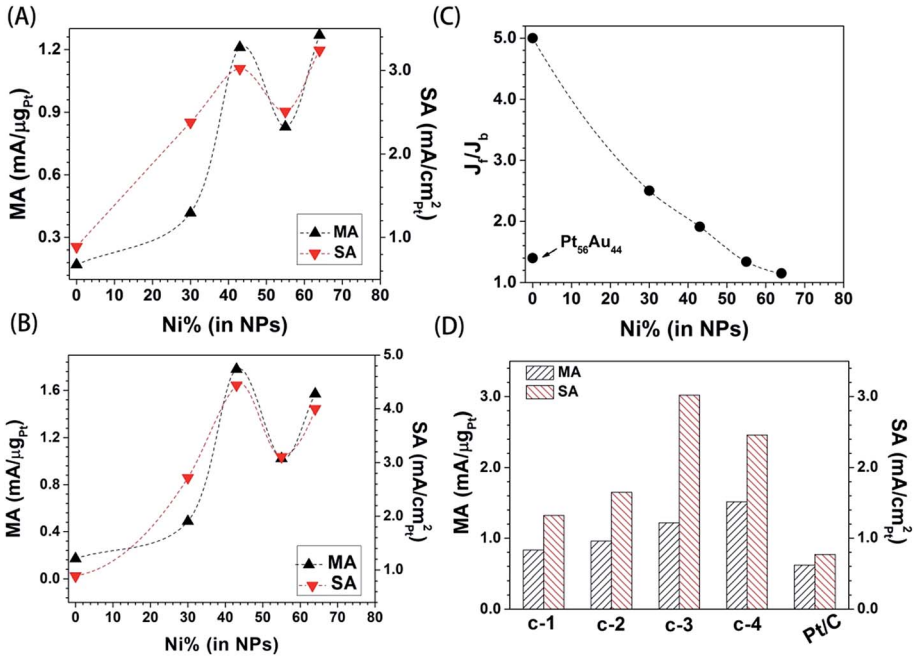

Fig. 9 Plots of MA and SA at a peak potential of 0.6 V (A) and at peak potential forward sweep (B), as well as J_f/J_b (C) as a function of Ni% for 400 °C/H_2 treated $Pt_{\sim 40}Au_xNi_{\sim 60-x}$/C; (D) comparison of MA and SA (at 0.6 V) for $Pt_{39}Au_{18}Ni_{43}$/C after different treatments: (c-1) 260 °C/O_2, (c-2) 177 °C/O_2, (c-3) 400 °C/H_2, and (c-4) 400 °C/H_2 treatment and potential cycling to 1.39 V.

with the Ni atomic percentage. Note that J_f/J_b for $Pt_{56}Au_{44}$/C shows a low value. The presence of Ni in PtAu clearly increased the tolerance to the carbonaceous species, in addition to the ability of surface Au atoms to suppress the carbonaceous species (Fig. S17†).

As shown in Fig. 9D for $Pt_{39}Au_{18}Ni_{43}$/C, the MA shows a clear increase in comparison with Pt/C. Sample c-4 exhibited a larger ECA and MA but smaller SA than c-3, indicating surface Pt enrichment for c-4 and a stronger negative charge sink effect.[47] Ni leaching leads to a smaller SA for c-4. For 400 °C/H_2 treated $Pt_{56}Au_{44}$/C (Fig. S18†), the MA is lower than that for the 260 °C/O_2 treated $Pt_{56}Au_{44}$/C. Potential cycling to a higher potential increases both SA and MA for the 400 °C/H_2 treated sample. The fact that the activities of $Pt_{56}Au_{44}$/C and $Pt_{38}Au_{62}$/C are much lower than that of $Pt_{39}Au_{18}Ni_{43}$/C indicates the important role of Ni in the PtAu NPs in terms of catalytic synergy.

In comparison with most binary catalysts reported in the literature (see Table S1†), catalysts studied here showed much enhanced performances. For example, the SA ratio for our $Pt_{39}Au_{18}Ni_{43}$/C *vs.* Pt/C is 3.92 with a J_f/J_b of 1.91, which is much larger than that of $Pt_{50}Au_{50}$ (SA ratio 2.2 with a J_f/J_b of 1.1).[6] For PtNi ribbons, the MA *vs.* Pt/C and J_f/J_b values are much lower than those of $Pt_{39}Au_{18}Ni_{43}$/C.[17] The MA and SA for hollow PtCu NPs are 3.73 and 4.46 times higher than those for Pt/C, whereas its J_f/J_b value is 1.0, which is much lower than that of $Pt_{39}Au_{18}Ni_{43}$/C.

The stability of the $Pt_{39}Au_{18}Ni_{43}$/C catalysts was also investigated (Fig. S19A and B†). For Samples c-4 and c-3 after a decrease in the first 30 potential cycles, the MA was found to remain unchanged at above 1.8 and 1.4 mA μg_{Pt}^{-1}. For Samples c-1 and c-2, the MA showed a decrease in the first 15 cycles and remained unchanged at about 1.1 and 1.2 mA μg_{Pt}^{-1}. The J_f/J_b remained largely unchanged in comparison with Pt/C. These results demonstrate that the high stability could be maintained with an optimal level of Ni in the AuPt nanoparticles. A detailed investigation of the stability evolution process is beyond the scope of this report, which will be reported in the near future.

3.4. Changes in the surface composition

It is evident that the MOR activities of $Pt_{39}Au_{18}Ni_{43}$/C catalysts depend strongly on the electrochemical and thermochemical treatments, which were examined by XPS to assess the surface electronic structure and composition. Fig. 10A and B show a set of XPS spectra in the Ni $2p_{3/2}$ region. By spectral deconvolution, there are three peak components of Ni 2p: peak (I) (light blue curves) can be ascribed to Ni^0 alloyed with Pt; peak (II) (pink curves) as well as the satellite peaks (III) (dark yellow curves) correspond to Ni–O species.[48–50] Sample c-1 shows a strong Ni–O peak, and Sample c-2 shows a weaker Ni–O peak. Ni–O is favored by O_2 treatment. Peaks (II) and (III) of the O_2 treated Samples c-1 and c-2 were greatly suppressed after potential cycling (Fig. 10B), indicating the removal of Ni–O species.

The deconvolution of Pt 4f spectra yields two sets of peaks (Fig. 10C and D): the first set corresponds to Pt^0 $4f_{7/2}$ and Pt^0 $4f_{5/2}$ and the second, with a shift on the right shoulder, can be ascribed to PtO $4f_{7/2}$ and PtO $4f_{5/2}$.[50,51] As shown in Fig. 10E and F, the deconvolution of the Au $4f_{7/2}$ and Au $4f_{5/2}$ spectra also yields two sets of peaks (84.29 and 84.66 eV, and 88.0 and 88.37 eV with the same FWHM of 0.65 eV, except for the untreated $Pt_{39}Au_{18}Ni_{43}$/C, whose FWHM is 1.0 eV). In the region of Au $4f_{7/2}$,[52] the ratio of peak areas at 84.66 and 84.29 eV is 0.52, 0.62, 0.38, and 1.34 for Samples c-1, c-2, c-3, and c, respectively. Due to lower coordination

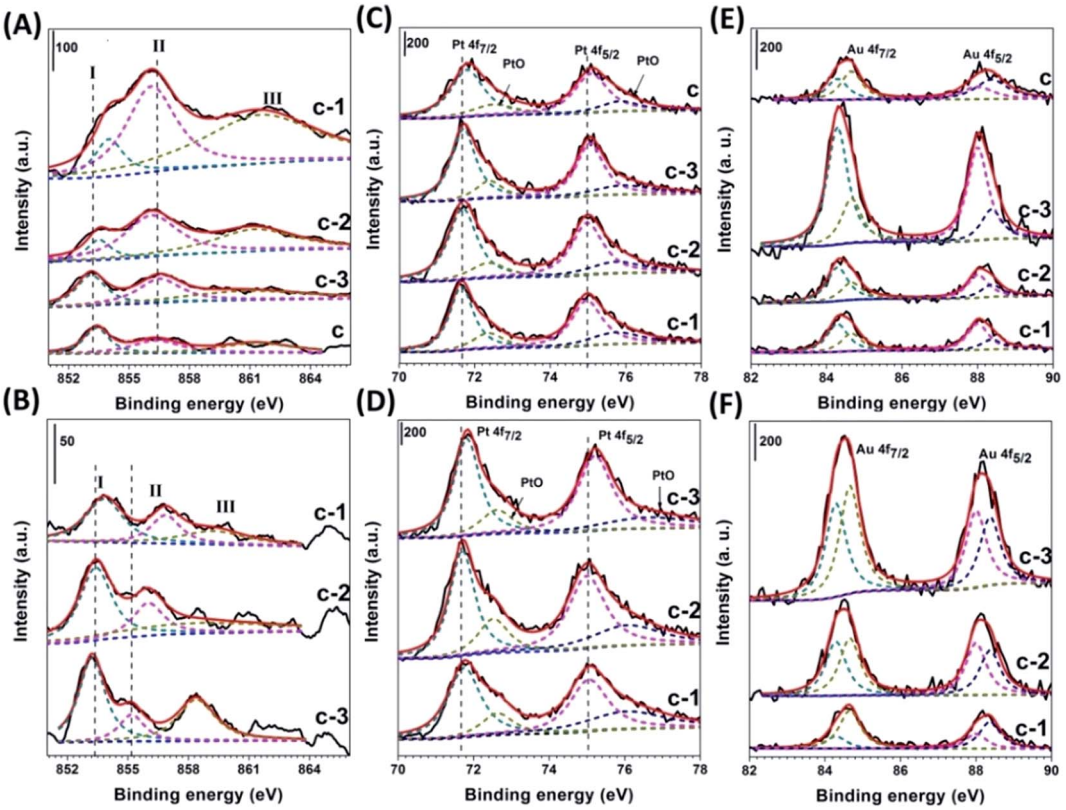

Fig. 10 XPS spectra (and deconvoluted peaks) for (c) the as-synthesized and (c-1) 260 °C/O_2, (c-2) 177 °C/O_2, and (c-3) 400 °C/H_2 treated $Pt_{39}Au_{18}Ni_{43}$/C, in regions of Ni 2p (A and B), Pt 4f (C and D), and Au 4f (E and F), before (A, C, and E) and after (B, D, and F) cycling at 50 mV s^{-1} between −0.20 and 1.25 V in 0.1 M $HClO_4$ for 10 cycles.

of the surface atoms, surface Au atoms exhibit a lower BE band than those underneath them.[53] After potential cycling, the ratios were shown to increase significantly to 3.16, 1.06, and 1.15 for Samples c-1, c-2, and c-3, reflecting the oxidation of considerable Au atoms, which promotes the MOR effectively.

Based on the XPS analysis of the peak areas of Pt 4f, Au 4f, and Ni 2p (Table S2†), the relative surface compositions were found to be $Pt_{57}Au_{14}Ni_{28}$, $Pt_{35}Au_{14}Ni_{50}$, $Pt_{50}Au_{20}Ni_{30}$, and $Pt_{42}Au_{42}Ni_{16}$ for Samples c, c-1, c-2, and c-3, respectively. The untreated sample showed less surface Ni and Au content compared to the bulk composition. This observation is consistent with a core–shell structure with Ni interior and Pt surface enrichments. Sample c-3 shows a significantly higher Au content than the bulk composition and an equal surface composition of Pt and Au, which is consistent with the HAADF-STEM mapping results. Because of the surface energy difference (fcc Au < fcc Pt < fcc Ni), the diffusions of Au atoms from the core to the shell and Ni atoms from the shell to the core were favored during thermal treatment under H_2, leading to the transformation of the Au-rich core/PtNi-rich shell structure to the Ni-rich core/PtAu-rich shell structure. After potential cycling, the relative surface compositions of Samples c-1, c-2, and c-3 were found to be $Pt_{57}Au_{28}Ni_{14}$, $Pt_{66}Au_{22}Ni_{11}$, and $Pt_{50}Au_{40}Ni_{10}$, showing 72%, 63%, and 37% loss of surface Ni compared to those before the cycling. It appeared that the PtAu-rich surface inhibits Ni leaching during potential cycling.

The Ni $2p_{3/2}$ peak (I) for sample c-1 appears at 854.00 eV, higher than 853.50 eV and 853.10 eV for Samples c-2 and c-3. The peak (II) position for Sample c-3 is higher than those of O_2 treated c-1 and c-2. After potential cycling, the Ni $2p_{3/2}$ peak (I) for all samples shifted negatively corresponding to the removal of surface Ni–O. Different from Ni^0 2p, the peak positions for Pt^0 $4f_{7/2}$ and $4f_{5/2}$, and Au $4f_{7/2}$ and $4f_{5/2}$ are shown to be shifted positively after potential cycling, indicative of the positively charged surface PtAu species. The Pt^0 $4f_{7/2}$ and $4f_{5/2}$ peak positions change in the order of c-3 > c-2 > c-1, whereas the Au $4f_{7/2}$ and $4f_{5/2}$ peak positions of Sample c-3 are lower than those of Samples c-1 and c-2. The surface Pt in Sample c-3 appears to undergo the most electron charge transfer to the neighboring Au atoms, leading to d-charge depletion and thus increasing the d-holes of Pt. The Pt with a higher d-charge depletion tends to show higher activity in catalyzing the MOR. In our previous study, the Pt $4f_{7/2}$ and Pt $4f_{5/2}$, and Au $4f_{7/2}$ and Au $4f_{5/2}$ for 400 °C/H_2 treated $Pt_{78}Au_{22}$/C were found at 71.9 and 75.25, and 84.45 and 88.10 eV, respectively,[54] which were more positive than those of Samples c-1, c-2 and c-3.

3.5. Mechanistic consideration

Taken together, the trimetallic PtAuNi NPs have been shown to undergo surface reconstruction by thermochemical and electrochemical treatments in terms of relative surface enrichment

and alloying, which have played an important role in enhancing the electrocatalytic performance for the MOR. Scheme 1 depicts the structural evolution of $Pt_{39}Au_{18}Ni_{43}$ NPs, which occurs during the thermochemical treatment and potential cycling. For the 400 °C/H_2 treatment, Au atoms move towards the surface, promoting the formation of the PtNi alloy. Note that PtNi NPs with a ~1 : 1 Pt : Ni ratio are the most active for the formation of the PtNi alloy in acidic solution.[55] Under the O_2 treatment (Scheme S2†), the formation of surface Ni–O species induces the diffusion of Ni atoms toward the surface. The partially oxidized Ni species would suppress the formation of the PtNi alloy. In the potential cycling, a great part of surface Ni atoms on the O_2-treated $Pt_{39}Au_{18}Ni_{43}$ NPs dissolves, whereas for the 400 °C/H_2 treated $Pt_{39}Au_{18}Ni_{43}$ NPs the Ni dissociation was suppressed by the surface Au and PtAu components with positive partial charges.

To understand the composition-driven optimization of activity for $Pt_{\sim 40}Au_{60-n}Ni_{\sim n}$, DFT calculations were performed based on small PtAuNi cluster models of different compositions ($Pt_4Au_{6-n}Ni_n$ clusters (n = 1–6)) after optimization. Molecular adsorption of CH_3OH on the model clusters was evaluated on the basis of the optimal bridge or atop adsorption model (Fig. 11). The results from geometry optimization of the clusters revealed that the Au atom tends to occupy the vertex site and the Ni atom the bridge site. The computational results showed that the CH_3OH molecule prefers to adsorb on the Pt atop site of the model clusters *via* the O atom. The variation of the adsorption energy of CH_3OH on the clusters *vs.* the cluster composition is shown in Fig. 11, revealing two lowest adsorption energies corresponding to the clusters of $Pt_{40}Au_{20}Ni_{40}$ and $Pt_{40}Ni_{60}$. It is evident that the trend in this plot coincides with the trend observed for the MOR activity. Generally speaking, if two reactants share the same transition state, the reactant with a higher adsorption energy would have a higher reaction barrier. Therefore, the adsorption of CH_3OH on $Pt_4Au_{6-n}Ni_n$ clusters with a higher adsorption energy could have a lower activity. Apparently, for $CH_3OH/Pt_{40}Au_{20}Ni_{40}$ and $CH_3OH/Pt_{40}Ni_{60}$, the lower adsorption energy means a higher activity. As shown in Fig. 11, this theoretical finding is clearly in agreement with the experimental data.

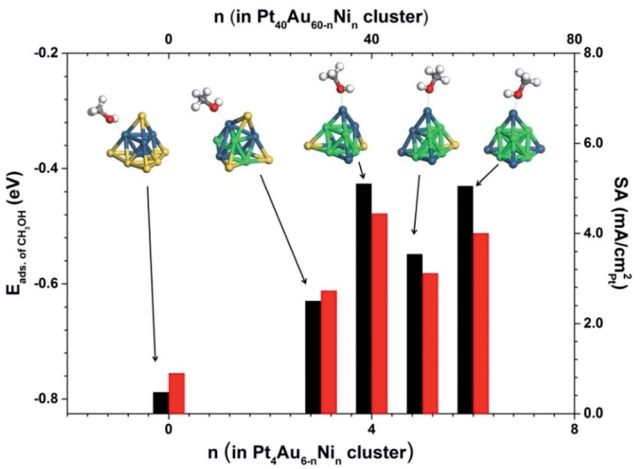

Fig. 11 Plot of the DFT-calculated adsorption energy for CH_3OH adsorbed on $Pt_4Au_{6-n}Ni_n$ clusters (n = 1–6) (black bar) and SA of the forward peak (red bar) *vs.* the normalized composition, with the corresponding $CH_3OH/Pt_4Au_{6-n}Ni_n$ structures shown in the top panel.

Considering the surface evolution and catalytic activity for the 400 °C/H_2 treated $Pt_{39}Au_{18}Ni_{43}$ NPs and the lowest reaction energy determined by the DFT calculation for the MOR in terms of the predominant indirect pathway,[56,57] Scheme 2 depicts a possible sequence of the formation of surface species that could be linked to the surface catalytic sites and synergy, including CH_3OH_{ad}, CH_2OH_{ad}, $CHOH_{ad}$, CHO_{ad}, and CO_{ad}. In terms of cleavage of C–H and O–H bonds of methanol, the activation could be favored by the shrinking of the Pt–Pt interatomic distance as a result of the PtNi alloying. The electrons generated in each of the dehydrogenation stages could be extracted by the neighboring surface Au atoms with partial positive charges. In contrast to a strong triple bond between CO and Pt[57] which poisons the catalytic sites, the CO species on Pt sites could be removed to the Au sites forming a weaker adsorption bond atop, which is reminiscent of the role of Au in AuPt nanoparticles for the MOR.[20] For the NPs with a surface atomic ratio of Pt : Au ~ 1 : 1 obtained after electrochemical activation, there is an optimal activity for the MOR. The transfer

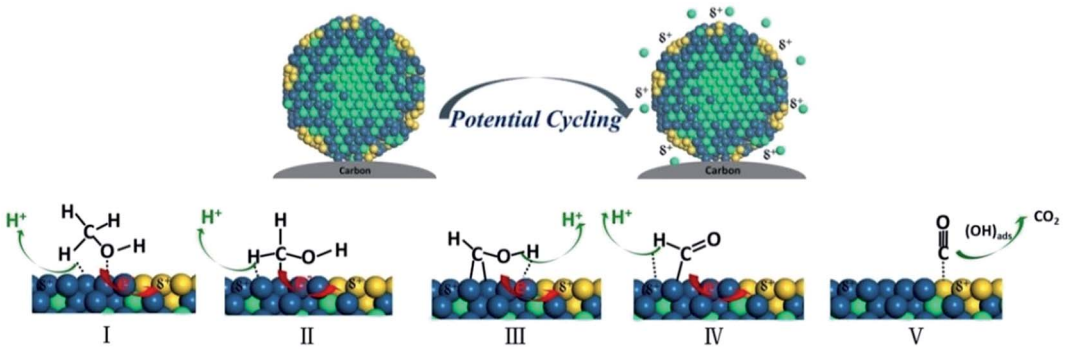

Scheme 2 Top panel: an illustration of the surface reconstruction of 400 °C/H_2 treated $Pt_{39}Au_{18}Ni_{43}$ NPs upon electrochemical potential cycling. Bottom panel: a possible sequence of the formation of surface species that could be linked to the surface catalytic sites and synergy (CH_3OH_{ad} (I), CH_2OH_{ad} (II), $CHOH_{ad}$ (III), CHO_{ad} (IV), and CO_{ad} (V)) in an indirect pathway for the electrocatalytic MOR over the catalyst.

of CO species to the Au site is followed by reaction with OH_{ad} species toward the formation of the CO_2 product. In these processes, the partially-positive charged Au sites serve to enable maneuvering of the electrons involved in the oxidation reactions. Moreover, the transfer of electrons from Ni with a lower electronegativity (1.91) to Pt with a higher electronegativity (2.28) in the PtNi alloy would lower the d-band center of Pt,[17,58,59] which suppresses the strong adsorption of carbonaceous species in each step. It is the introduction of Ni into the bimetallic NPs that has produced the above multifunctional synergy involving shrinking of Pt–Pt distances for enhancing the dehydrogenation and surface enrichments of Au and PtNi alloy phases for effective removal of surface carbonaceous species and maneuvering of the electrons. We note that a detailed study of the CO oxidation on PtAuNi is part of our ongoing investigation, which will be reported in the near future.

4. Conclusion

In conclusion, we have demonstrated that the introduction of a third low-cost nickel into AuPt nanoparticles followed by thermochemical and electrochemical tuning leads to a significant enhancement of the catalytic activity for the methanol oxidation reaction. The unique combination of composition-controlled synthesis and thermochemical/electrochemical reconstruction of metal components on the surface and in the interior of the nanoparticles has enabled the tuning of electrocatalytic properties. In comparison with the general approach to design catalysts based on the bimetallic PtAu NPs, the introduction of Ni into the bimetallic NPs is shown to produce a significant multifunctional synergy. This synergy involves alloying of Ni with Pt to shrink the Pt–Pt distances which enhances the catalytic dehydrogenation, and to induce surface enrichment of Au which promotes the effective removal of surface carbonaceous species and enables the Au atoms to function as an electron sink for maneuvering of the electrons involved in the oxidation reaction. To achieve the multifunctionality, the thermochemical and electrochemical treatments of the core–shell PtAuNi NPs are shown to contribute to the controllability of the surface enrichment that plays a critical role in the electrocatalytic enhancement. The thermochemical treatment under hydrogen favors surface enrichment of Au and core enrichment of Ni, which increase the efficiency of the noble metal in the alloy, optimize the d-band electronic properties of Pt, and promote the multifunctional synergy. The experimentally observed electrocatalytic activity of the nanocatalysts in terms of Ni doping in PtAu nanoparticles is further supported by the results of theoretical analysis of the adsorption energy of methanol on the nanoclusters, revealing that the higher activity correlates well with the lower adsorption energy. These findings have provided new insights into the design and preparation of highly active electrocatalysts. We also note that an expansion of this work to the study of the structural modifications of the catalysts for other electrocatalytic reactions, *e.g.*, oxygen reduction reaction,[60–63] is also an important direction of future studies.

Conflicts of interest

There are no conflicts to declare.

Acknowledgements

This work was supported by DOE-BES Grant (DE-SC0006877) and NSF Grant (CHE 1566283). AL acknowledges the support from China Postdoctoral Science Foundation Grant (2017M622077). SY acknowledges the support from IEEC. The authors thank Professor David Jenkins of Binghamton University for his great help in the XRD measurements.

References

1 X. M. Ren, P. Zelenay, S. Thomas, J. Davey and S. Gottesfeld, *J. Power Sources*, 2000, **86**, 111–116.
2 D. Chu and R. Jiang, *Solid State Ionics*, 2002, **148**, 591–599.
3 U. A. Paulus, U. Endruschat, G. J. Feldmeyer, T. J. Schmidt, H. Bonnemann and R. J. Behm, *J. Catal.*, 2000, **195**, 383–393.
4 E. Antolini, *Mater. Chem. Phys.*, 2003, **78**, 563–573.
5 G. Q. Lu and A. Wieckowski, *Curr. Opin. Colloid Interface Sci.*, 2000, **5**, 95–100.
6 J. Suntivich, Z. Xu, C. E. Carlton, J. Kim, B. Han, S. W. Lee, N. Bonnet, N. Marzari, L. F. Allard, H. A. Gasteiger, K. Hamad-Schifferli and S.-H. Yang, *J. Am. Chem. Soc.*, 2013, **135**, 7985–7991.
7 J. Luo, P. N. Njoki, Y. Lin, D. Mott, L. Wang and C. J. Zhong, *Langmuir*, 2006, **22**, 2892–2898.
8 C. Lu, W. Kong, H. Zhang, B. Song and Z. Wang, *J. Power Sources*, 2015, **296**, 102–108.
9 R. Meyer, C. Lemire, S. K. Shaikhutdinov and H.-J. Freund, *Gold Bull.*, 2004, **37**, 72–124.
10 J. Luo, M. M. Maye, Y. Lou, L. Han, M. Hepel and C. J. Zhong, *Catal. Today*, 2002, **77**, 127–138.
11 M. M. Maye, Y. Lou and C. J. Zhong, *Langmuir*, 2000, **16**, 7520–7523.
12 V. Petkov, B. N. Wanjala, R. Loukrakpam, J. Luo, L. Yang, C. J. Zhong and S. Shastri, *Nano lett.*, 2012, **12**, 4289–4299.
13 Z. Borkowska, A. Tymosiak-Zielinska and R. Nowakowski, *Electrochim. Acta*, 2004, **49**, 2613–2621.
14 H. Tang, J. H. Chen, M. Y. Wang, L. H. Nie, Y. F. Kuang and S. Z. Yao, *Appl. Catal., A*, 2004, **275**, 43–48.
15 M. Umeda, H. Ojima, M. Mohamedi and I. J. Uchida, *J. Power Sources*, 2004, **136**, 10–15.
16 J. R. Kitchin, J. K. Nørskov, M. A. Barteau and J. G. Chen, *J. Chem. Phys.*, 2004, **120**, 16613–16617.
17 C. Xu, J. Hou, X. Pang, X. Li, M. Zhu and B. Tang, *Int. J. Hydrogen Energy*, 2012, **37**, 10489–10498.
18 A. B. A. A. Nassr, I. Sinev, M.-M. Pohl, W. Grünert and M. Bron, *ACS Catal.*, 2014, **4**, 2449–2462.
19 S. Papadimitriou, S. Armyanov, E. Valova, A. Hubin, O. Steenhaut, E. Pavlidou, G. Kokkinidis and S. Sotiropoulos, *J. Phys. Chem. C*, 2010, **114**, 5217–5223.
20 D. Mott, J. Luo, P. N. Njoki, Y. Lin, L. Wang and C. J. Zhong, *Catal. Today*, 2007, **122**, 378–385.

21 J. Luo, M. M. Maye, N. N. Kariuki, L. Wang, P. Njoki, Y. Lin, M. Schadt, H. R. Naslund and C. J. Zhong, *Catal. Today*, 2005, **99**, 291–297.
22 L. Yang, W. Yang and Q. Cai, *J. Phys. Chem. C*, 2007, **111**, 16613–16617.
23 J.-M. Yan, X.-B. Zhang, T. Akita, M. Haruta and Q. Xu, *J. Am. Chem. Soc.*, 2010, **132**, 5326–5327.
24 J. Luo, L. Wang, D. Mott, P. N. Njoki, Y. Lin, T. He, Z. Xu, B. N. Wanjana, I.-I. S. Lim and C. J. Zhong, *Adv. Mater.*, 2008, **20**, 4342–4347.
25 J. Zhang, K. Sasaki, E. Sutter and R. R. Adzic, *Science*, 2007, **315**, 220–222.
26 B. N. Wanjala, J. Luo, R. Loukrakpam, B. Fang, D. Mott, P. N. Njoki, M. Engelhard, H. R. Naslund, J. K. Wu, L. Wang, O. Malis and C. J. Zhong, *Chem. Mater.*, 2010, **22**, 4282–4294.
27 C. Wang, D. Vliet, K. L. More, N. J. Zaluzec, S. Peng, S. Sun, H. Daimon, G. Wang, J. Greeley, J. Pearson, A. P. Paulikas, G. Karapetrov, D. Strmcnik, N. M. Markovic and V. R. Stamenkovic, *Nano Lett.*, 2011, **11**, 919–926.
28 Z. Cai, Z. Lu, Y. Bi, Y. Li, Y. Kuang and X. Sun, *Chem. Commun.*, 2016, **52**, 3903–3906.
29 Y. Kang, J. Snyder, M. Chi, D. Li, K. L. More, N. M. Markovic and V. R. Stamenkovic, *Nano Lett.*, 2014, **14**, 6361–6367.
30 Q. Shi, C. Zhu, S. Fu, D. Du and Y. Lin, *ACS Appl. Mater. Interfaces*, 2016, **8**, 4739–4744.
31 X. Sun, D. Li, Y. Ding, W. Zhu, S. Guo, Z. L. Wang and S. Sun, *J. Am. Chem. Soc.*, 2014, **136**(15), 5745–5749.
32 X. Tan, S. Prabhudev, A. Kohandehghan, D. Karpuzov, G. A. Botton and D. Mitlin, *ACS Catal.*, 2015, **5**, 1513–1524.
33 A. Dutta and J. Ouyang, *ACS Catal.*, 2015, **5**, 1371–1380.
34 C. Xu, J. Hou, X. Pang, X. Li, M. Zhu and B. Tang, *Int. J. Hydrogen Energy*, 2012, **37**, 10489–10498.
35 E. Zhu, Y. Li, C.-Y. Chiu, X. Huang, M. Li, Z. Zhao, Y. Liu, X. Duan and Y. Huang, *Nano Res.*, 2016, **9**, 149–157.
36 L.-L. Shen, G.-R. Zhang, S. Miao, J. Liu and B.-Q. Xu, *ACS Catal.*, 2016, **6**, 1680–1690.
37 Y. Wu, D. Wang, G. Zhou, R. Yu, C. Chen and Y. Li, *J. Am. Chem. Soc.*, 2014, **136**, 11594–11597.
38 J. Wan, Y. L. Fan, D. W. Gong, S. G. Shen and X. Q. Fan, *Model. Simul. Mater. Sci. Eng.*, 1999, **7**, 189–206.
39 L. Yang, S. Shan, R. Loukrakpam, V. Petkov, Y. Ren, B. N. Wanjala, M. H. Engelhard, J. Luo, J. Yin, Y. Chen and C. J. Zhong, *J. Am. Chem. Soc.*, 2012, **134**, 15048–15060.
40 J. Wu, S. Shan, V. Petkov, B. Prasai, H. Cronk, P. Joseph, J. Luo and C. J. Zhong, *ACS Catal.*, 2015, **5**, 5317–5327.
41 M. R. Xia, W. Ding, K. Xiong, L. Li, X. Q. Qi, S. G. Chen, B. S. Hu and Z. D. Wei, *J. Phys. Chem. C*, 2013, **117**, 10581–10588.
42 S. Zhang, S. Guo, H. Zhu, D. Su and S. Sun, *J. Am. Chem. Soc.*, 2012, **134**, 5060–5063.
43 V. Petkov, S. Shan, P. Chupas, J. Yin, L. Yang, J. Luo and C. J. Zhong, *Nanoscale*, 2013, **5**, 7379–7387.
44 B. Fang, J. Luo, P. N. Njoki, R. Loukrakpam, D. Mott, B. Wanjala, X. Hu and C. J. Zhong, *Electrochem. Commun.*, 2009, **11**, 1139–1141.
45 E. Herrero, W. Chrzanowski and A. Wieckowski, *J. Phys. Chem.*, 1995, **99**, 10423–10424.
46 S. Rousseau, O. Marie, P. Bazin, M. Daturi, S. Verdier and V. Harle, *J. Am. Chem. Soc.*, 2010, **132**, 10832–10841.
47 A. Lu, D.-L. Peng, F. Chang, Z. Skeete, S. Shan, A. Sharma, J. Luo and C. J. Zhong, *ACS Appl. Mater. Interfaces*, 2016, **8**, 20082–20091.
48 A. Lu, Y. Chen, H. Li, A. Dowd, M. B. Cortie, Q. Xie, H. Guo, Q. Qi and D.-L. Peng, *Int. J. hydrogen energy*, 2014, **39**, 18919–18928.
49 M. Caffio, B. Cortigiani, G. Rovida, A. Atrei and C. Giovanardi, *J. Phys. Chem. B*, 2004, **108**, 9919–9926.
50 Y. Shen, K. Xiao, J. Xi and X. Qiu, *J.Power Sources*, 2015, **278**, 235–244.
51 Y. Luo, A. Habrioux, L. Calvillo, G. Granozzi and N. Alonso-Vante, *Chem. Phys. Chem.*, 2014, **15**, 2136–2144.
52 A. S. Walton, J. Fester, M. Bajdich, M. A. Arman, J. Osiecki, J. Knudsen, A. Vojvodic and J. V. Lauritsen, *ACS Nano*, 2015, **9**, 2445–2453.
53 P. Heimann, J. F. van der Veen and D. E. Eastman, *Solid State Commun.*, 1981, **38**, 595–598.
54 B. N. Wanjala, J. Luo, B. Fang, D. Mott and C. J. Zhong, *J. Mater. Chem.*, 2011, **21**, 4012–4020.
55 R. Loukrakpam, J. Luo, T. He, Y. Chen, Z. Xu, P. N. Njoki, B. N. Wanjala, B. Fang, D. Mott, J. Yin, J. Klar, B. Powell and C.-J. Zhong, *J. Phys. Chem. C*, 2011, **115**, 1682–1694.
56 T. Iwasita, *Electrochimi. Acta*, 2002, **47**, 3663–3674.
57 M. Neurock, M. Janik and A. Wieckowski, *Faraday Discuss.*, 2008, **140**, 363–378.
58 K.-W. Park, J.-H. Choi, B.-K. Kwon, S.-A. Lee and Y.-E. Sung, *J. Phys. Chem. B*, 2002, **106**, 1869–1877.
59 W. Gordy and W. J. O. Thomas, *J. Chem. Phys.*, 1956, **24**, 439–444.
60 H. M. Barkholtz and D.-J. Liu, *Mater. Horiz.*, 2017, **4**, 20–37.
61 C. Zhang, R. Zhang, L. Li and X. Li, *Chen W. Part. Part. Syst. Charact.*, 2017, **34**, 1700034.
62 S. Fu, C. Zhu, J. Song, M. H. Engelhard, B. Xiao, D. Du and Y. Lin, *Chem. Eur. J.*, 2017, **23**, 10460–10464.
63 D. Rossouw, L. Chinchilla, N. Kremliakova and G. A. Botton, *Part. Part. Syst. Charact.*, 2017, **34**, 1700051.